Original Research

Time-Resolved 3D MR Velocity Mapping at 3T: Improved Navigator-Gated Assessment of Vascular Anatomy and Blood Flow

Michael Markl, PhD,[1]* Andreas Harloff, MD,[2] Thorsten A. Bley, MD,[1] Maxim Zaitsev, PhD,[1] Bernd Jung, PhD,[1] Ernst Weigang, MD,[3] Mathias Langer, MD, MBA,[1] Jürgen Hennig, PhD,[1] and Alex Frydrychowicz, MD[1]

Purpose: To evaluate an improved image acquisition and data-processing strategy for assessing aortic vascular geometry and 3D blood flow at 3T.

Materials and Methods: In a study with five normal volunteers and seven patients with known aortic pathology, prospectively ECG-gated cine three-dimensional (3D) MR velocity mapping with improved navigator gating, real-time adaptive k-space ordering and dynamic adjustment of the navigator acceptance criteria was performed. In addition to morphological information and three-directional blood flow velocities, phase-contrast (PC)-MRA images were derived from the same data set, which permitted 3D isosurface rendering of vascular boundaries in combination with visualization of blood-flow patterns.

Results: Analysis of navigator performance and image quality revealed improved scan efficiencies of 63.6% ± 10.5% and temporal resolution (<50 msec) compared to previous implementations. Semiquantitative evaluation of image quality by three independent observers demonstrated excellent general image appearance with moderate blurring and minor ghosting artifacts. Results from volunteer and patient examinations illustrate the potential of the improved image acquisition and data-processing strategy for identifying normal and pathological blood-flow characteristics.

Conclusion: Navigator-gated time-resolved 3D MR velocity mapping at 3T in combination with advanced data processing is a powerful tool for performing detailed assessments of global and local blood-flow characteristics in the aorta to describe or exclude vascular alterations.

Key Words: phase-contrast MRI; flow; velocity mapping; aorta; vascular hemodynamics
J. Magn. Reson. Imaging 2007;25:824–831.

MODERN EQUIPMENT AND IMAGING TECHNIQUES based on the intrinsic sensitivity of MRI to flow and motion offer the possibility of acquiring spatially registered functional information simultaneously with morphological data within a single experiment. Characterizing the dynamic components of blood flow and cardiovascular function can provide insights into normal and pathological physiology, and considerable progress in this field has been made in recent years (1–5).

ECG synchronized time-resolved three-dimensional (3D) MR-velocity mapping (also termed phase-contrast (PC)-MRI) offers investigators the opportunity to assess 3D blood-flow characteristics with true 3D and temporal coverage of a cardiovascular region of interest (ROI). Several scientific and clinical applications have already been reported (6–14). However, previous implementations and data-analysis strategies suffered from nonexistent or insufficient respiration control and related artifact generation (8,11), limited signal-to-noise ratio (SNR) (13), and the lack of a comprehensive 3D visualization of vasculature and hemodynamics (7,9).

Qualitative and quantitative assessments of blood flow using PC-MRI have been performed over the past few years, and the technique has been validated extensively (15–17). Recent phantom studies have confirmed the accuracy of time-resolved 3D MR velocity mapping in comparison with 2D PC flow measurement (14) and optical methods (18).

In time-resolved 3D data acquisitions, the large amounts of data necessitate measurement durations that often exceed normal human breath-holding capabilities. To avoid artifacts related to breathing motion, such as ghosting or image blurring, a method for respiration control is a prerequisite for good diagnostic image quality. A potential solution is offered by the application of navigator gating (19–23). For 3D data acquisition with three-directional velocity encoding, however, navigator gating using typical acceptance windows of 4–8 mm would result in unacceptably long

[1]Department of Diagnostic Radiology, Medical Physics, University Hospital Freiburg, Freiburg, Germany.
[2]Department of Neurology and Clinical Neurophysiology, University Hospital Freiburg, Freiburg, Germany.
[3]Department of Cardiovascular Surgery, University Hospital Freiburg, Freiburg, Germany.
Contract grant sponsor: Deutsche Forschungsgemeinschaft; Contract grant number: MA 2383/3-1.
*Address reprint requests to: M.M., Department of Diagnostic Radiology, Medical Physics, University Hospital Freiburg, Hugstetter Strasse 55, 79106 Freiburg, Germany.
E-mail: michael.markl@uniklinik-freiburg.de
Received January 18, 2006; Accepted October 13, 2006.
DOI 10.1002/jmri.20871
Published online 7 March 2007 in Wiley InterScience (www.interscience.wiley.com).

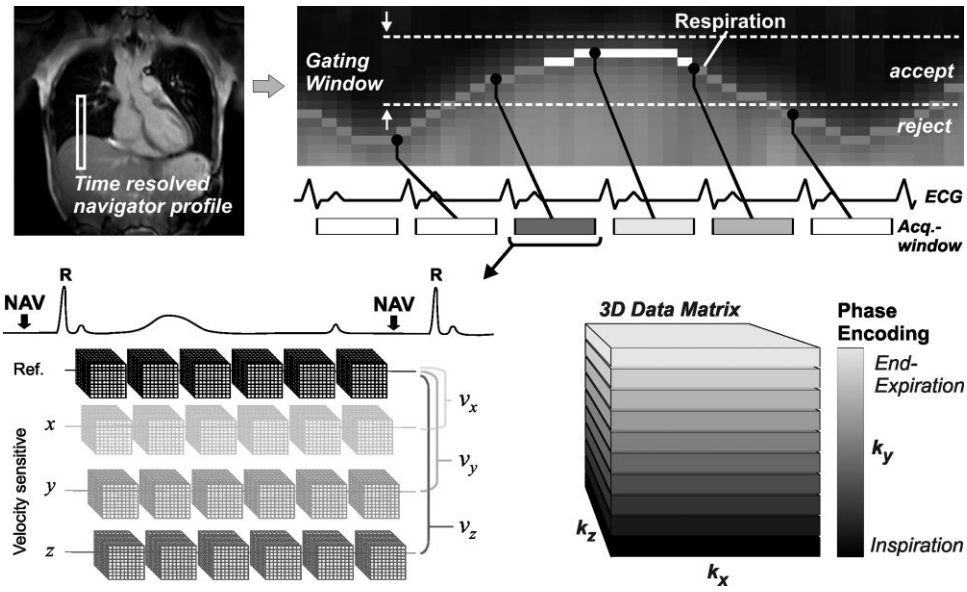

Figure 1. Schematic illustration of respiration control by adaptive navigator gating and prospective ECG gating. For each time frame a flow-compensated reference data set (Ref.) and three separate flow-sensitive 3D volumes (flow sensitization in x, y, and z) were successively collected. Three-directional blood flow velocities (v_x, v_y, and v_z) were calculated by subtracting the flow-sensitized data from the reference volumes. The late diastolic navigator signal (NAV) of the lung–liver interface was used for prospective respiration estimation. Data within the acceptance range were sorted into k-space according to their respiratory position, as schematically indicated for differently gray-shaded sections of 3D k-space (lower right).

scan times or insufficient spatial resolution. Furthermore, scan durations of tens of minutes may give rise to drifts or sudden changes in the navigator profile that may, in the worst case, lead to a restart of examinations or loss of incomplete data sets.

Hence, in this study we sought to improve navigator-gated time-resolved 3D MR velocity mapping based on real-time adaptive k-space reordering in combination with a wider data acceptance window (12–14 mm) and dynamic adjustment of the navigator acceptance window with increased navigator efficiency (24).

The selection of the gating window and the resulting scan efficiency is driven by the requirement that respiration artifacts should be minimized as much as possible, while the total scan time should be tolerable for patients. We performed semiquantitative grading of diagnostic image quality and level of artifact generation in order to test the practicability of the proposed method in routine patient examinations.

Orientation within a four-dimensional (4D) data set may be difficult to achieve, and readily identifiable anatomical landmarks are desirable for faster image interpretation and flow visualization. Therefore, we additionally combined 3D blood-flow visualization with geometric information of the vasculature derived from the same data set. 3D angiographic data were imported into the flow-visualization package and used to aid further 3D blood-flow analysis by improved identification of the vessel or ROI (25).

MATERIALS AND METHODS

Human Subjects

Five healthy volunteers (two males and three females, mean age = 29.8 years, age range = 23–41 years) and seven patients (two males and five females, mean age = 40.1 years, age range = 23–66 years) were included in this study. Written informed consent was obtained from all subjects prior to the MRI investigation. The study was approved by the local ethics committee.

MRI

MR System and Imaging Parameters

All examinations were performed on a 3T system (TRIO; Siemens, Erlangen, Germany). Images were acquired using an eight-channel phased-array body coil. 3D MR velocity mapping data were acquired using a k-space segmented 3D RF-spoiled gradient-echo sequence with interleaved three-directional velocity encoding (14).

Measurements were performed during free breathing and were prospectively gated to the ECG cycle. For each 3D cine time frame, the velocity encodings for the four acquisitions (reference and three velocity-sensitive scans) were executed consecutively for two k-space lines (segmentation factor = 2) along the phase-encoding direction, resulting in a temporal resolution of 8TR = 48.8 msec (see Fig. 1). The number of reconstructed cardiac phases varied between 11 and 15 according to the subject's heart rate.

Additional imaging parameters were $\alpha = 15°$, velocity sensitivity (venc) = 150 cm/second, TE = 3.5–3.7 msec, TR = 6.1 msec, bandwidth = 480–650 Hz/pixel. For 11 subjects, 3D MR velocity mapping data were acquired in a sagittal oblique 3D volume, rectangular FOV = (230–300 × 340–400) mm^2, with a slab thickness of 66–112 mm that included the entire thoracic aorta and the proximal parts of the supra-aortic branches with a spatial resolution of (2.4–4.0 × 1.6–2.1 × 3.0–5.0) mm^3. An additional volunteer examination (spatial res-

Table 1
Scoring System for the Evaluation of Different Image Quality Categories in Adaptively Gated 3D MR Velocity Mapping Data Sets

Category	Feature		Score
	Description	Present?	
General appearance	Clear delineation of aortic wall	Yes	1
		No	0
	Sufficient lumen contrast	Yes	1
		No	0
	Supra-aortic branches visible	Yes	1
		No	0
	Dynamics of aortic wall motion evident	Yes	1
		No	0
Ghosting	None		3
	Mild: clear depiction of aortic lumen		2
	Moderate: interference with aortic lumen		1
	Severe		0
Blurring	None		2
	Moderate: blurred aortic wall		1
	Severe		0

olution = 3.0 × 1.6 × 3.0 mm^3) was performed in coronal orientation covering the entire abdominal aorta, aortic bifurcation, and left and right iliac arteries.

Respiration Control

A navigator signal to detect the lung–liver boundary was acquired during late diastole within each cardiac cycle (measurement time = 15 msec, evaluation time = 10 msec). To improve scan efficiency, respiration control was achieved by a combination of navigator gating with a wide acceptance window (12–14 mm) and adaptive k-space reordering. If respiration was within the preselected navigator acceptance window, the acquired data were phase-encoded according to their respiratory position (similarly to the previously reported respiratory-ordered phase encoding (ROPE) technique (24)), as schematically indicated for differently gray-shaded sections in Fig. 1.

To overcome the problem of possible lung–liver boundary drifts, the navigator acceptance window was dynamically adapted to changes in the respiration pattern. For each RR interval, the positions of the lung–liver interfaces of the past 32 cardiac cycles were compared and the maximum diaphragm position was extracted. If changes occurred in the maximum diaphragm position (i.e., respiration drifts), the entire position of the acceptance window was shifted in real time. The navigator window boundaries (white dashed lines in Fig. 1) were readjusted such that the new maximum diaphragm position was located in the center of the navigator window, while the navigator window width was maintained.

Analysis of Image Quality

Image quality was semiquantitatively evaluated by three independent readers (two experienced radiologists and one MR physicist) based on grading of the morphological images (magnitude data) derived from the 3D velocity mapping data set.

The image grading system was designed to accommodate features representing the general appearance of the aorta in combination with a focus on ghosting and blurring potentially introduced by insufficient respiration control. To evaluate the general appearance on a scale of 0–4, the readers were asked to grade images according to clear delineation of the aortic wall, sufficient lumen contrast, identifiable supra-aortic branches (mesenteric branches of the abdominal aorta in one subject), and depiction of the dynamics of aortic wall motion. Further, the severity of respiration-induced ghosting and blurring, and their effect on the appearance of aortic lumen and wall were evaluated on four- and three-point scales, respectively. A more detailed description of the grading system is given in Table 1.

Interobserver agreement was evaluated separately for each image grading category for pairs of readers. Average agreement was calculated for all possible pairs.

Data Processing and 3D Blood-Flow Visualization

Data reconstruction on the scanner included averaging of all four magnitude images of the differently flow-encoded data, as well as calculation of three-directional velocity images (see Fig. 1). In a next step all reconstructed source phase difference images underwent fully automated noise filtering and eddy-current correction based on strategies introduced by Walker et al (26), which required approximately 10 minutes.

In addition, we used magnitude and filtered velocity images from three volunteers and two patients to generate time-resolved 3D PC-MRA data by calculating absolute velocity images $I_i^{PC-MRA}(\vec{r})$ with background suppression by magnitude weighting according to:

$$I_i^{PC-MRA}(\vec{r}) = I_i^{Mag}(\vec{r}) \sqrt{\sum_{j=x,y,z} v_{j,i}^2(\vec{r})}, \quad i = 1, \ldots, N \qquad (1)$$

where $\vec{r}$ is the spatial location within the 3D volume, j represents the velocity encoding direction in image coordinates (x = read, y = phase, z = slice), and i is the measured time frame within the cardiac cycle out of a total number of N frames. Magnitude and velocity im-

Table 2
Total Scan Time, Scan Efficiency for Adaptively Navigator-Gated Data Acquisition, and Semiquantitatively-Evaluated Image Quality for Healthy Volunteers ($N = 5$) and Patients ($N = 7$)*

	Total scan time (minutes) mean ± SD (minimum/maximum)	Scan efficiency (%) mean ± SD (minimum/maximum)	Image quality (poor–excellent)		
			Appearance (0-4)	Ghosting (0-3)	Blurring (0-2)
Normal volunteers	20.0 ± 2.1 (17.0/22.0)	68.3 ± 9.7 (60.0/79.6)	3.3 ± 0.8	1.7 ± 0.7	1.1 ± 0.5
Patients	20.1 ± 6.9 (15.0/32.0)	60.5 ± 10.7 (47.1/77.4)	3.6 ± 0.7	2.1 ± 0.6	1.0 ± 0.3
All subjects	20.1 ± 5.3 (15.0/32.0)	63.6 ± 10.5 (47.1/79.6)	3.44 ± 0.73	1.92 ± 0.69	1.03 ± 0.38

*Variability of average values is indicated as ± 1 standard deviation (SD).

ages are denoted by I_i^{Mag} and v, respectively. To further enhance vascular regions with high flow and suppress background signal, an additional time-independent PC-MRA data set was generated as the squared sum of the individual 3D PC-MRA images:

$$I_{WS}^{PC-MRA}(\vec{r}) = \frac{1}{N}\sum_{i=1}^{N} I_i^{PC-MRA}(\vec{r})^2 \qquad (2)$$

Finally, all reconstructed data were loaded into a commercially available software package (EnSight; CEI, Apex, NC, USA) for interactive 3D data analysis. Bloodflow visualization included velocity vector graphs, 3D stream lines (traces tangent to the velocity field of an individual time frame) and time-resolved 3D particle traces (path of massless particles) (27,28). In addition, thresholding of the PC-MRA data was employed to generate a semitransparent 3D isosurface representation of the vascular anatomy.

RESULTS

Total Scan Time, Scan Efficiency, and Image Quality

Adaptive navigator gating with a mean scan efficiency of 63.6% ± 10.5% (range = 47.1–79.6%) was successfully performed for all examinations. Both scan efficiency and total scan time (20.1 ± 5.3 minutes) exhibited a greater variability in patient examinations, indicating increased variation in the overall heart rate and the respiration patterns (Table 2, left columns). Dynamic adjustment of the navigator acceptance window resulted in stable scan efficiencies even for noticeable changes in the respiration patterns.

A summary of the grading results for normal volunteers and patients is given in Table 2 (right columns). A comparison of the different categories used for image grading reveals excellent general image appearance (average grading = 3.44 ± 0.73) with moderate blurring (average grading = 1.92 ± 0.69) and only minor ghosting artifacts (average grading = 1.03 ± 0.38). No severe ghosting artifacts were seen, and the general image appearance received at least a grading of 2 (a typical raw magnitude image of the thoracic aorta is shown in Fig. 2, left). Interobserver agreement was fair for general image appearance (72%) and blurring (61%), and reduced for the evaluation of ghosting (44%), resulting in an overall average agreement of 59%.

Normal Volunteers

In all of the healthy volunteers, generally unsuspicious blood flow and no complex flow patterns were seen. 3D particle traces over time (Fig. 2) illustrate the complete spatial and temporal coverage of vascular anatomy and hemodynamics in the entire thoracic aorta. The combi-

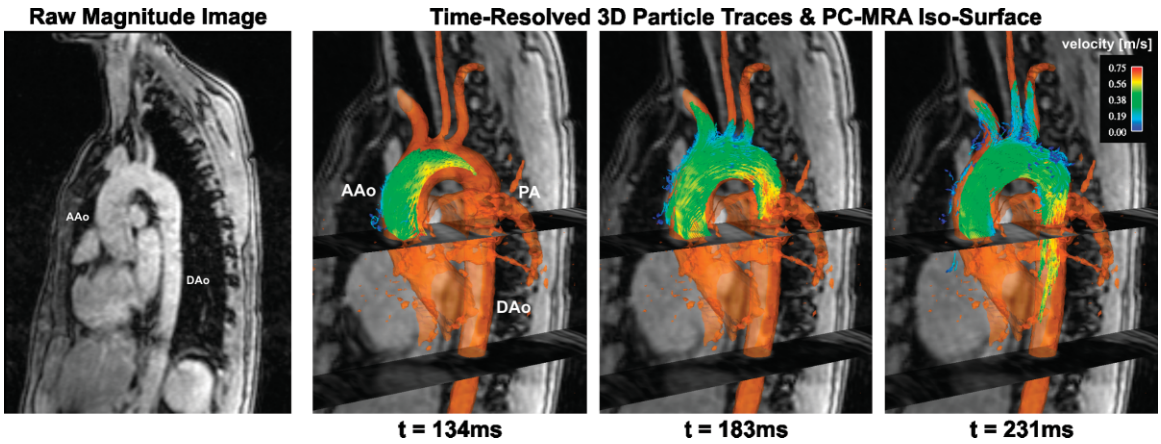

Figure 2. Left: Raw magnitude image illustrating the level of typical blurring and ghosting associated with the adaptive navigator gating approach. Right: Temporal evolution of 3D particle traces for a healthy volunteer representing three-directional blood flow in the in the ascending aorta (AAo), aortic arch, and distal descending thoracic aorta (DAo), and the distribution in the supra-aortic branches. The times listed below the individual images correspond to the time between R-wave detection and data acquisition. Color coding and tracer length represent the local absolute velocities.

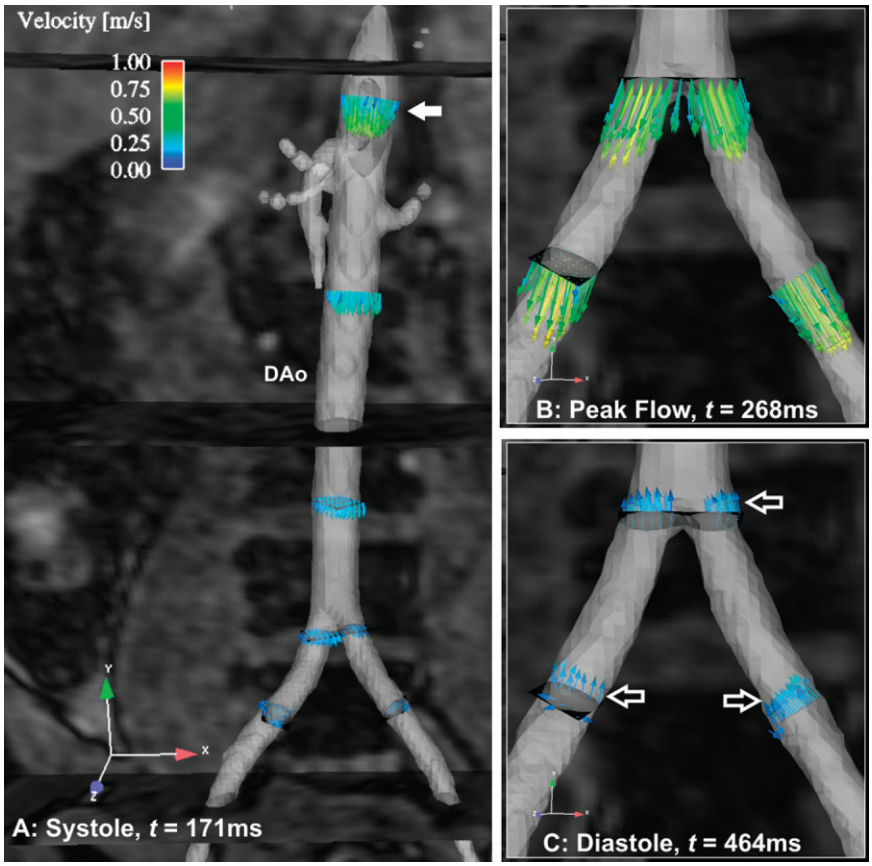

Figure 3. Blood-flow visualization in the abdominal aorta (DAo), aortic bifurcation, and iliac arteries in a healthy volunteer for three different time frames within the cardiac cycle. Interactive placement of 2D vector graphs was aided by the semitransparent 3D isosurface generated from squared-sum PC-MRA data.

nation with a systolic PC-MRA data set allows for improved anatomical orientation and identification of individual vascular segments.

Note the excellent image quality with respect to respiration artifacts (i.e., absence of ghosting, and only minor blurring) in the morphological image (Fig. 2, left) from the same 3D MR velocity mapping data set, which received high grades for general appearance as well as respiration artifact level by all three readers.

From Fig. 3 it is evident that the isosurface display of the squared-sum PC-MRA aids in the identification of vascular ROIs and, more specifically, the retrospective placement of 2D cut planes for the visualization of local blood-flow patterns. Velocity vector fields in 2D cut planes normal to the vascular lumen at multiple locations were used to visualize the dynamics and shape of flow profiles in the abdominal aorta and iliac arteries. As expected from physiology, flow profiles in the upper part of the abdominal aorta exhibit high velocities and parabolic flow profiles during early systole (Fig. 3a, solid white arrow), while flow profiles further downstream are gradually less developed. However, a subsequent time frame (90 msec later) illustrates simultaneous filling of both iliac arteries and fully developed flow profiles during peak flow, indicating the ability to visualize pulse wave propagation (Fig. 3b). Additionally, diastolic retrograde flow can be clearly appreciated in Fig. 3c (open white arrows). Although overall image appearance was rated as rather poor (average grading = 2), respiration artifacts were graded as moderate for blurring (average grading = 1) and mild–moderate for ghosting (average grading = 1.3), and did not severely impair the vector field visualization of the velocity data.

Patients

In contrast to the results from the volunteer examinations, patients with pathological geometric changes of the thoracic aorta revealed considerable flow alterations.

Changes in local blood-flow patterns were identified in a 48-year-old patient with an asymptomatic and mild stenosis in the left proximal subclavian artery but otherwise normal aortic geometry, as confirmed by contrast-enhanced (CE)-MRA (Fig. 4). The value of a spatially coregistered PC-MRA isosurface for identifying the corresponding vascular segment in the 3D MR velocity mapping data set can be clearly appreciated. 3D visualization of blood flow in the same region demonstrate marked flow acceleration through the luminal narrowing (arrow), while other vascular regions show no disturbances in 3D blood-flow characteristics. The clear delineation of morphological structures in the background images also reflects the low respiration artifact level for this data set.

Figure 5 shows visualization results for a 36-year-old patient who underwent a bypass connecting the ascending aorta and proximal descending aorta due to symptomatic aortic coarctation. The location and extent of the bypass relative to the thoracic aorta were successfully visualized using PC-MRA isosurfacing, and the findings assisted in the interactive placement

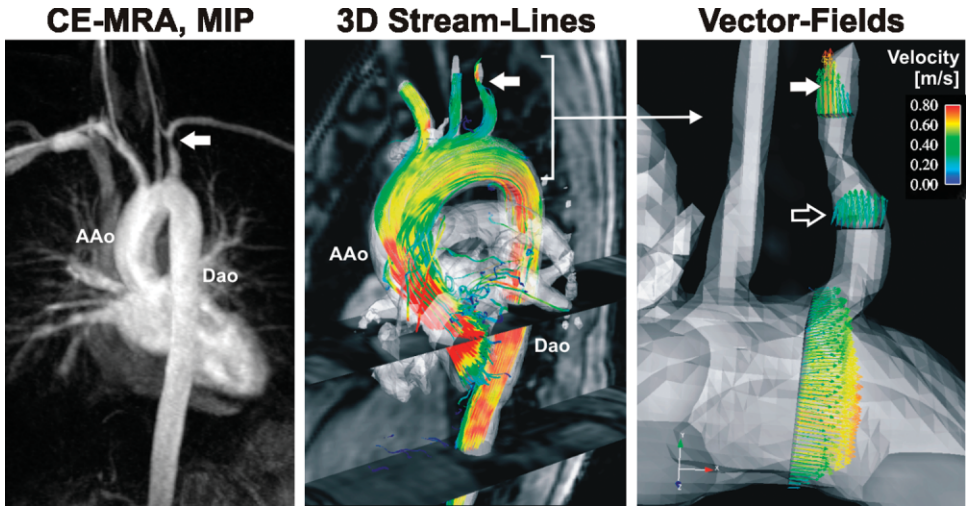

Figure 4. Vascular geometry and hemodynamics for a patient with a mild stenosis in the left proximal subclavian artery as shown by CE-MRA (left, arrow). 3D PC-MRA data (gray-shaded semitransparent isosurface) in conjunction with 3D stream lines (middle) permit the 3D depiction of systolic blood flow within the entire thoracic aorta, which already indicates flow alteration due to luminal narrowing (solid arrow). Systolic velocity vector fields placed in the aortic arch and left subclavian artery (right) illustrate marked flow acceleration within and directly distal to the stenosis (solid arrow) compared to flow profiles before the stenosis (open arrow).

of the oblique cut planes for vector graph visualization to assess bypass function (Fig. 5, left). High flow through the bypass (open black arrow) and substantially reduced flow through the original aortic arch (solid white arrow) can be clearly appreciated in the magnified part of the 3D volume (Fig. 5, right). General image appearance was also graded as excellent for this data set, with a mild increase in ghosting compared to Fig. 4.

Additional findings for other patients included accelerated flow patterns in luminal narrowing caused by thrombosis, complex and retrograde flow characteristics for type-A dissection, marked helix formation in the descending aorta in a patient with graft repair, complex vertical flow in an ascending aortic aneurysm, and flow acceleration in graft repair of the ascending aorta.

DISCUSSION

The results from volunteer and patient examinations underline the feasibility of our 3D MR-velocity mapping approach at 3T for evaluating local and global blood-flow characteristics. Specifically, the utility of combin-

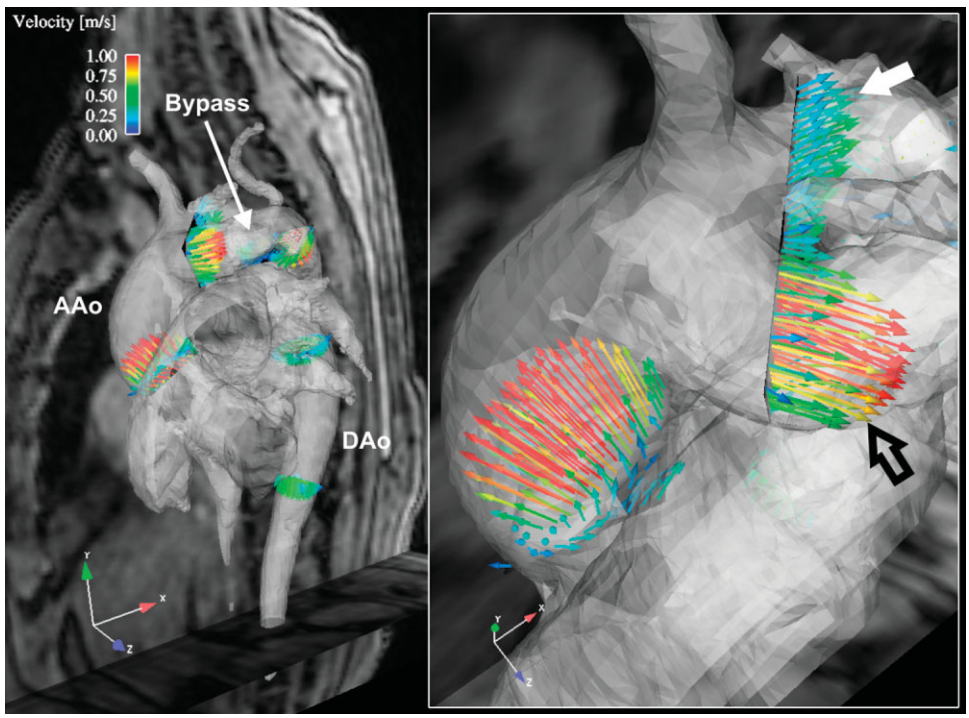

Figure 5. Vector graph visualization of systolic flow profiles in a patient with aortic coarctation and a bypass connecting the aortic arch and proximal descending aorta. Both flow channels (original aortic arch and bypass) were well visualized using 3D PC-MRA data. Systolic velocity profiles clearly indicate high flow through the bypass (open black arrow) and considerably reduced flow through the aortic arch (solid white arrow).

ing PC-MRA (vascular boundaries by 3D isosurface generation) and advanced data visualization to evaluate blood-flow changes associated with vascular pathology was demonstrated in patients with stenosis and aortic bypass.

Additionally, adaptive navigator gating with relatively wide acceptance windows and compensation for potential drifts in the respiration pattern kept overall scan times at acceptable levels while allowing for improved temporal resolution compared to previously reported studies (13,14,28). Scan efficiencies on the order of 65% were achieved, and thus exceed typical values (30–50%) based on narrow acceptance windows of 6–8 mm obtained in previous studies (19–21).

To evaluate the effects on image quality and artifact level (respiratory-induced blurring and ghosting), three independent observers performed semiquantitative image grading. The results revealed overall good image appearance and low artifact levels with relatively low variability of the mean image grading, as indicated by the low standard deviations (SDs), and thus demonstrate the feasibility (i.e., improved scan efficiency with only minor respiration artifacts) of our implementation.

A drawback of our implementation is related to the basic principle of adaptive gating (i.e., phase encoding as a function of the respiration position). As a result, some residual blurring and thus degradation of spatial resolution is unavoidable. While respiratory ghosting was mostly rated as minor, and in some cases could even be eliminated almost completely, the images were never entirely free of blurring, which was rated as at least moderate for all subjects.

Data from the volunteer examination of the abdominal aorta (Fig. 3) received the worst image rating with comparably strong blurring and ghosting. This may be related to peristalsis during the long scan time, which is difficult to remove by motion compensation because of the nonperiodic nature of bowel movement. Pharmaceutical relaxation agents (e.g., butyl scopolamine-bromide) could be applied in future studies to compensate for such effects.

It should be noted that several other options for implementing the navigator approach are available, but were not explored in this study. For example, data could be acquired during the entire respiration cycle without navigator gating and only adaptive k-space ordering. Such an approach would result in 100% scan efficiency at the probable expense of increased respiratory ghosting and blurring. Furthermore, no comparison of navigator gating with and without the inclusion of adaptive k-space ordering was performed.

Navigator tracking (i.e., adjustment of the position 3D data volume relative to the respiration phase) is a promising technique that has the potential to further reduce ghosting and blurring; however, it was not available with our current implementation.

Further studies are needed to evaluate the performance of different respiration control techniques and to investigate how the acquired blood flow velocities and subsequent visualization and postprocessing strategies are affected by different levels of blurring and ghosting.

To keep the total scan time tolerable for patients, restrictions must be imposed on the maximum achievable spatial and/or temporal resolution. Parallel imaging techniques, such as sensitivity encoding (SENSE) and generalized autocalibrating partially parallel acquisition (GRAPPA), have great potential for reducing the total scan time and/or improving spatial and temporal resolution; however, to date they are not part of our scan protocol (29). Recent studies have reported a considerable gain in SNR and reduced velocity noise for PC flow measurements at 3T (30). Specifically, the combination with parallel imaging is promising because high-field MRI may compensate for the SNR loss associated with parallel imaging (31). Future methodological studies will focus on the investigation and implementation of parallel imaging techniques.

The creation of PC-MRA data clearly aided data processing by simplifying the identification of vascular segments for subsequent visualization of local flow features. After the PC-MRA and time-resolved 3D flow data were loaded into the visualization software package, an easily performed, fast 3D isosurface function was employed to generate an overview over the vascular geometry (see Figs. 2–5) within a few seconds. Without PC-MRA, a 2D cut-plane transecting the magnitude data in different orientations had to be generated and moved through the 3D data set to identify vascular ROIs, which was much more cumbersome and required substantially longer processing times on the order of minutes.

A potential limitation of PC-MRA generation may be related to the predefined velocity sensitivity of the 3D velocity mapping acquisition, which is selected to exceed the expected peak velocities in the aorta to avoid velocity aliasing. As a consequence, regions with low flow may suffer from low signal in the PC-MRA data and thus lead to impaired depiction of vascular geometry if isosurface generation based on thresholding is used. In addition, the squared-sum averaging process used to calculate the PC-MRA data may result in blurred vascular geometry as a result of motion of the vascular lumen during the cardiac cycle. However, even if the diastolic and systolic positions of the artery of interest are substantially different, reduced diastolic velocities will contribute to a lesser extent to the final image and may therefore result in only minor blurring (see Eq. [2]).

Although characteristic flow features related to normal and pathological arterial geometries were successfully analyzed in the presented study, it has to be noted that currently available software tools are limited in terms of a quantitative description of flow alterations. The implementation of further quantitative evaluation strategies (e.g., to assess flow rates, wall shear stress, and vorticity) is therefore warranted in order to develop and apply more objective diagnostic criteria for the description of vascular pathologies.

In conclusion, adaptively navigator-gated time-resolved 3D MR velocity mapping at 3T provided overall good image quality with moderate blurring and only minor ghosting artifacts. In addition, the results from the optimized data processing underline the potential of the presented method for identifying normal and local pathological blood-flow characteristics.

REFERENCES

1. Lima JA, Desai MY. Cardiovascular magnetic resonance imaging: current and emerging applications. J Am Coll Cardiol 2004;44: 1164–1171.
2. Pettigrew RI, Oshinski JN, Chatzimavroudis G, Dixon WT. MRI techniques for cardiovascular imaging. J Magn Reson Imaging 1999;10:590–601.
3. Nayler GL, Firmin DN, Longmore DB. Blood flow imaging by cine magnetic resonance. J Comput Assist Tomogr 1986;10:715–22.
4. Rebergen SA, van der Wall EE, Doornbos J, de Roos A. Magnetic resonance measurement of velocity and flow: technique, validation, and cardiovascular applications. Am Heart J 1993;126:1439–1456.
5. Pelc NJ, Herfkens RJ, Shimakawa A, Enzmann DR. Phase contrast cine magnetic resonance imaging. Magn Reson Q 1991;7:229–254.
6. Mohiaddin RH, Yang GZ, Kilner PJ. Visualization of flow by vector analysis of multidirectional cine MR velocity mapping. J Comput Assist Tomogr 1994;18:383–392.
7. Bogren HG, Mohiaddin RH, Yang GZ, Kilner PJ, Firmin DN. Magnetic resonance velocity vector mapping of blood flow in thoracic aortic aneurysms and grafts. J Thorac Cardiovasc Surg 1995;110: 704–714.
8. Wigstrom L, Sjoqvist L, Wranne B. Temporally resolved 3D phase-contrast imaging. Magn Reson Med 1996;36:800–803.
9. Kilner PJ, Yang GZ, Wilkes AJ, Mohiaddin RH, Firmin DN, Yacoub MH. Asymmetric redirection of flow through the heart. Nature 2000;404:759–761.
10. Fyrenius A, Wigstrom L, Ebbers T, Karlsson M, Engvall J, Bolger AF. Three dimensional flow in the human left atrium. Heart 2001; 86:448–455.
11. Bogren HG, Buonocore MH, Valente RJ. Four-dimensional magnetic resonance velocity mapping of blood flow patterns in the aorta in patients with atherosclerotic coronary artery disease compared to age-matched normal subjects. J Magn Reson Imaging 2004;19: 417–427.
12. Kvitting JP, Ebbers T, Wigstrom L, Engvall J, Olin CL, Bolger AF. Flow patterns in the aortic root and the aorta studied with time-resolved, 3-dimensional, phase-contrast magnetic resonance imaging: implications for aortic valve-sparing surgery. J Thorac Cardiovasc Surg 2004;127:1602–1607.
13. Markl M, Draney MT, Hope MD, et al. Time-resolved 3-dimensional velocity mapping in the thoracic aorta: visualization of 3-directional blood flow patterns in healthy volunteers and patients. J Comput Assist Tomogr 2004;28:459–468.
14. Markl M, Chan FP, Alley MT, et al. Time-resolved three-dimensional phase-contrast MRI. J Magn Reson Imaging 2003;17:499–506.
15. Rebergen SA, van der Wall EE, Doornbos J, de Roos A. Magnetic resonance measurement of velocity and flow: technique, validation, and cardiovascular applications. Am Heart J 1993;126;1439–1456.
16. Frayne R, Steinman DA, Ethier CR, Rutt BK. Accuracy of MR phase contrast velocity measurements for unsteady flow. J Magn Reson Imaging 1995;5:428–431.
17. Lee VS, Spritzer CE, Carroll BA, et al. Flow quantification using fast cine phase-contrast MR imaging, conventional cine phase-contrast MR imaging, and Doppler sonography: in vitro and in vivo validation. AJR Am J Roentgenol 1997;169:1125–1131.
18. Elkins CJ, Markl M, Iyengar A, Wicker R, Eaton J. Full field velocity and temperature measurements using magnetic resonance imaging in turbulent complex internal flows. Int J Heat Fluid Flow 2004;25:702–710.
19. Ehman RL, Felmlee JP. Adaptive technique for high-definition MR imaging of moving structures. Radiology 1989;173:255–263.
20. Firmin D, Keegan J. Navigator echoes in cardiac magnetic resonance. J Cardiovasc Magn Reson 2001;3:183–193.
21. Stuber M, Botnar RM, Danias PG, Kissinger KV, Manning WJ. Submillimeter three-dimensional coronary MR angiography with real-time navigator correction: comparison of navigator locations. Radiology 1999;212:579–587.
22. Kozerke S, Hasenkam JM, Pedersen EM, Boesiger P. Visualization of flow patterns distal to aortic valve prostheses in humans using a fast approach for cine 3D velocity mapping. J Magn Reson Imaging 2001;13:690–698.
23. Baltes C, Kozerke S, Atkinson D, Boesiger P. Retrospective respiratory motion correction for navigated cine velocity mapping. J Cardiovasc Magn Reson 2004;6:785–792.
24. Bailes DR, Gilderdale DJ, Bydder GM, Collins AG, Firmin DN. Respiratory ordered phase encoding (ROPE): a method for reducing respiratory motion artefacts in MR imaging. J Comput Assist Tomogr 1985;9:835–838.
25. Dumoulin CL. Phase contrast MR angiography techniques. Magn Reson Imaging Clin N Am 1995;3:399–411.
26. Walker PG, Cranney GB, Scheidegger MB, Waseleski G, Pohost GM, Yoganathan AP. Semiautomated method for noise reduction and background phase error correction in MR phase velocity data. J Magn Reson Imaging 1993;3:521–530.
27. Buonocore MH. Visualizing blood flow patterns using streamlines, arrows, and particle paths. Magn Reson Med 1998;40:210–226.
28. Wigström L, Ebbers T, Fyrenius A, et al. Particle trace visualization of intracardiac flow using time-resolved 3D phase contrast MRI. Magn Reson Med 1999;41:793–799.
29. Blaimer M, Breuer F, Mueller M, Heidemann RM, Griswold MA, Jakob PM. SMASH, SENSE, PILS, GRAPPA: how to choose the optimal method. Top Magn Reson Imaging 2004;15:223–236.
30. Lotz J, Doker R, Noeske R, et al. In vitro validation of phase-contrast flow measurements at 3 T in comparison to 1.5 T: precision, accuracy, and signal-to-noise ratios. J Magn Reson Imaging 2005;21:604–610.
31. Pruessmann KP. Parallel imaging at high field strength: synergies and joint potential. Top Magn Reson Imaging 2004;15:237–244.